IVYSPRING INTERNATIONAL PUBLISHER

International Journal of Biological Sciences

2027; 23(1): 42-58. doi: 10.7150/ijbs.136334

Research Paper

Targeting PYCR2-PP2Ac-eIF2α Axis Enhances the Efficacy of *KRAS*^{G12D} Inhibition in Cholangiocarcinoma

Huibo Feng[1†], Mengmiao Pei[2†], Mengyou Xu[1†], Xinhao Xing[3], Zhongning Yu[4], Xinzhu Quan[3], Lu Chen[3], Yunkai Lin[3], Yufei Pan[3], Taiyu Shang[3], Yuanyuan Zhang[3], Liwei Dong[3,5✉], Tianyi Jiang[3✉], Hongyang Wang[1,2,3,5✉]

1. Peking University Cancer Hospital, Peking University, Beijing, 100142, China.
2. Department of Hepatobiliary Surgery, Eastern Hepatobiliary Surgery Hospital, Naval Medical University, Shanghai, 201800, China.
3. National Center for Liver Cancer, Naval Medical University, No. 366 Qianju Road, Jiading, Shanghai, 201800, China.
4. Key Laboratory for Advanced Materials and Joint International Research Laboratory of Precision Chemistry and Molecular Engineering, Feringa Nobel Prize Scientist Joint Research Center, School of Chemistry and Molecular Engineering, Frontiers Center for Materiobiology and Dynamic Chemistry, East China University of Science and Technology, Shanghai, 200237, China.
5. Laboratory of Signaling Regulation and Targeting Therapy of Liver Cancer, the Ministry of Education, No. 225 Changhai Road, Yangpu, Shanghai, 200438, China.

†These authors contributed equally to this work.

✉ Corresponding authors: Liwei Dong, dlw@smmu.edu.cn; Tianyi Jiang, jiangtianyi@smmu.edu.cn; Hongyang Wang, hywangk@vip.sina.com.

© 2027 The Author(s). This is an open access article distributed under the Creative Commons Attribution 4.0 International Licence, subject to the Publisher's Terms of Use at https://ivyspring.com/terms.

Received: 2026.04.16; Accepted: 2026.09.11; Published: 2027.01.01

Abstract

KRAS mutations occur in a considerable proportion of cholangiocarcinoma (CCA), with *KRAS*^{G12D} being the predominant subtype. Although *KRAS*^{G12D} inhibitors, including MRTX1133, HRS-4642 and GFH375, have shown promising activity, therapeutic responses remain limited by diverse resistance mechanisms. Using a CRISPR-Cas9 loss-of-function screen, we identified pyrroline-5-carboxylate reductase 2 (PYCR2) as a previously unrecognized regulator of *KRAS*^{G12D} inhibitor sensitivity. PYCR2 was significantly upregulated in MRTX1133-resistant cells, and its depletion markedly augmented the anti-tumor efficacy of MRTX1133 *in vitro* and *in vivo*. Notably, this effect was independent of its canonical function in proline metabolism. Mechanistically, PYCR2 interacted with eukaryotic translation initiation factor 2α (eIF2α) and facilitated its dephosphorylation via recruiting the catalytic subunit of protein phosphatase 2A (PP2Ac). This signaling cascade sustains global protein translation and supports tumor cell survival under *KRAS*^{G12D} inhibition. Targeting this axis, either by genetic depletion of PYCR2 or pharmacological blockade of eIF2α dephosphorylation using Salubrinal, significantly enhanced the antitumor efficacy of MRTX1133 in cellular models and xenograft tumors. Collectively, our findings uncover that the PYCR2-PP2Ac-eIF2α axis serves as a promising target for improving the efficacy of *KRAS*^{G12D}-targeted therapy in CCA.

Keywords: *KRAS*^{G12D}, MRTX1133, PYCR2, eIF2α, PP2Ac, cholangiocarcinoma

Introduction

Cholangiocarcinoma (CCA) is a heterogeneous biliary tract cancer originating from the biliary epithelium. It is frequently diagnosed at an advanced stage, contributing to poor clinical outcomes [1]. Despite surgical resection being the only potentially curative strategy, most patients are ineligible at the time of diagnosis due to late presentation [2]. For advanced disease, the current standard of treatment involves combination therapy with gemcitabine, cisplatin, and the immune checkpoint inhibitors, a regimen that represents a significant shift from traditional chemotherapy. While this approach has improved survival outcomes compared to chemotherapy alone, the overall benefit remains modest, and most patients still experience disease progression [3, 4]. Low response rates and the rapid emergence of resistance are common, highlighting a critical unmet need for more effective therapeutic strategies.

Among potential therapeutic targets in CCA, oncogenic mutations in the *KRAS* gene are prevalent, with *KRAS*^{G12D} being a major subtype [5]. The

development of selective inhibitors, such as MRTX1133, has provided new opportunities for targeting $KRAS^{G12D}$-driven tumors [6], demonstrating potent antitumor activity in preclinical models. However, growing evidence indicates that both intrinsic and acquired resistance substantially limits its therapeutic efficacy [7]. Tumor cells evade *KRAS* inhibition through diverse adaptive alterations, including reactivation of downstream signaling activity, such as epithelial-to-mesenchymal transition and SMARCB-MYC network-driven mesenchymal reprogramming [8, 9]. Despite these advances, the key molecular factors that determine sensitivity or resistance to MRTX1133 in CCA remain unclear, hindering the development of rational combination strategies.

Metabolic enzymes have long been regarded as regulators of cellular bioenergetics and biosynthesis. However, emerging evidence indicates that many metabolic enzymes possess noncanonical functions that contribute to tumor progression and therapeutic response [10, 11]. In this study, we performed a CRISPR-Cas9 loss-of-function screen, targeting 2333 drug targets, kinases and phosphatases related genes, to identify key regulators of MRTX1133 sensitivity in CCA. We identified pyrroline-5-carboxylate reductase 2 (PYCR2), a key enzyme in proline biosynthesis [12, 13], as a critical determinant of drug response and its depletion markedly enhanced the antitumor activity of MRTX1133 in both sensitive and resistant models. Notably, we found that PYCR2 was upregulated in MRTX1133-resistant cells and mediated resistance through a noncanonical, metabolism-independent mechanism. PYCR2 interacts with eukaryotic translation initiation factor 2α (eIF2α) and promotes its dephosphorylation via a protein phosphatase 2A catalytic subunit (PP2Ac)-dependent mechanism, thereby sustaining protein translation and tumor cell survival under $KRAS^{G12D}$ inhibition. These findings reveal a previously unrecognized noncanonical role for PYCR2 in regulating therapeutic response and highlight the PYCR2-PP2Ac-eIF2α pathway as a promising therapeutic target to overcome resistance to $KRAS^{G12D}$ inhibition in CCA.

Materials and Methods

Cell lines and cell culture

Human CCA cell lines (RBE, HCCC9810, CCLP-1, QBC939 and FRH-0201) and HEK-293T cells were purchased from the Shanghai Cell Bank of the Chinese Academy of Sciences, China. SK-CHA-1 was provided by H. You, Xiamen University. TFK1 and HuCCT1 cell lines were provided by S.-Q. Zou (Tongji Hospital, Huazhong University of Science and Technology). HCC3975 and 783C-6 cell lines were isolated from primary human CCA tissues by our laboratory. The KPT8 mouse cell line was isolated in our laboratory from CCA tumors of mice in a hydrodynamic tail vein-induced cancer model (SB13-luc+sg$PTEN$+$KRAS^{G12D}$). Cells were grown in RPMI-1640 supplemented with 10% FBS and 1% penicillin-streptomycin, and cultured at 37°C in a humidified 5% CO_2 incubator.

Mice

Male C57BL/6 mice and BALB/c nu/nu mice (6 weeks old), were purchased from GemPharmatech Biotechnology (Jiangsu, China) and housed under specific pathogen-free conditions.

Animal experiments

For subcutaneous xenograft assays, 1×10^6 CCA cells were injected subcutaneously into the right flank of 6-week-old male BALB/c nude mice or C57BL/6 mice. When tumors reached a measurable size (approximately 100 mm^3), mice were randomly assigned to indicated treatment groups. Tumor volume was monitored every 2-3 days by measuring tumor length and width with calipers, and tumor volume was calculated using the formula: length × $width^2$ /2. When tumor volume reached 1500 mm^3, mice were euthanized via CO_2 asphyxiation. At the experimental endpoint, tumors were excised, weighed, photographed, and processed for subsequent analyses. All animal experiments were conducted in accordance with protocols approved by the Ethics Board of EHBH.

CRISPR-Cas9 loss-of-function screen

Experiments were performed following previously described methods [14]. A pooled CRISPR-Cas9 sgRNA library targeting 2333 drug targets, kinases and phosphatases related genes, with 24569 sgRNAs, was introduced into HCC3975 cells via lentiviral infection at a low multiplicity of infection (MOI < 0.3) to achieve single sgRNA integration per cell. After puromycin selection, cells were allocated into control and treatment groups and exposed to DMSO, MRTX1133, or KRpep-2d for 7 days. Genomic DNA was subsequently isolated, and sgRNA were amplified by PCR and subjected to next-generation sequencing to determine sgRNA abundance. Genes enriched or depleted under drug selection were ranked based on sgRNA representation, and the top 8 candidate genes were selected for subsequent validation.

Establishment of MRTX1133-resistant cells

The MRTX1133-resistant HCC3975 cell line (HCC3975-R) was generated by stepwise adaptation of

parental HCC3975 cells to increasing doses of MRTX1133 over an extended period. The established resistant cells were maintained in medium supplemented with the maintenance concentration of MRTX1133 and were cultured in drug-free medium for a short recovery period before functional assays.

Drug sensitivity assay

Cell viability was assessed using a Cell Viability Assay Kit (Vazyme, DD1101) following the manufacturer's protocol. Briefly, 5000 cells per well were seeded into 96-well white-bottom plates. After cell attachment, cells were treated with serial dilutions of the indicated compounds for 72 h. Subsequently, CellTier reagent was diluted 1:1 with serum-free medium, and 100 µL of the mixture was added to each well. After incubation at 37°C for 15 min, luminescence signals were recorded using a microplate reader (Synergy H1, BioTek). All experiments were performed in triplicate. Cell viability was expressed as relative luminescence intensity normalized to the vehicle-treated control group. The half-maximal growth inhibitory concentration (GI_{50}) values were calculated by nonlinear regression analysis using GraphPad Prism 9.0.

Gene silencing and overexpression

Transient silencing of PYCR2, eIF2α, and PP2Ac was performed using specific siRNAs delivered with Lipo8000 transfection reagent (Beyotime) according to the manufacturers' instructions. All siRNA oligonucleotides were designed and synthesized by GenePharma (Shanghai, China). The corresponding sequences are provided in Supplementary Table S1.

Lentiviral constructs targeting PYCR2 were generated by GeneChem (Shanghai, China). The shRNA sequences were listed in data file S1. The shRNA-containing vectors were transduced into cancer cells via lentiviral infection in the presence of polybrene (4 µg/mL). After 48 h, infected cells were selected with puromycin (2 µg/mL), and knockdown efficiency was confirmed by quantitative PCR (qPCR) or immunoblot analysis.

Flag-tagged expression plasmids for PYCR2, eIF2α, and PP2Ac were purchased from Sino Biological (Shanghai, China) and introduced into cells using Lipo8000 transfection reagent.

Quantitative real-time PCR

Total RNA was isolated and converted into cDNA using a commercial reverse transcription kit. Quantitative PCR was conducted using SYBR Green master mix on a real-time PCR platform. Relative gene expression was normalized to GAPDH or ACTB.

Immunoblotting

Cells or tumor tissues were homogenized in RIPA lysis buffer containing protease and phosphatase inhibitors. Equivalent amounts of protein samples were separated by SDS-PAGE and transferred onto PVDF membranes. After blocking, membranes were incubated with specific primary antibodies at 4°C overnight, followed by incubation with HRP-linked secondary antibodies. Immunoreactive signals were detected using an enhanced chemiluminescence (ECL) system.

Colony formation assay

Cells were plated at a low seeding density in 6-well plates and exposed to the indicated treatments. After 10-14 days of incubation, colonies were fixed with paraformaldehyde and visualized by crystal violet staining. Colony numbers were quantified, normalized to the control group, and presented as relative values.

Apoptosis assay

Apoptotic cell death was assessed by Annexin V-FITC/propidium iodide (PI) staining followed by flow cytometry. Cells were harvested after the indicated treatments, stained according to the manufacturer's instructions, and analyzed using FlowJo software.

Cell cycle analysis

Cells were fixed with 70% ethanol at 4 °C overnight, followed by RNase A treatment and PI staining. DNA content was analyzed by flow cytometry, and the percentages of cells in G0/G1, S, and G2/M phases were quantified.

Measurement of intracellular ROS and mitochondrial ROS

Intracellular reactive oxygen species (ROS) levels were assessed using the fluorescent probe DCFH-DA. Briefly, cells were seeded in 6-well plates and subjected to the indicated treatments. After incubation, cells were washed with PBS and loaded with DCFH-DA working solution at 37 °C for 30 min in the dark. Following removal of unbound probe by washing, cells were collected and analyzed by flow cytometry. Mitochondrial ROS levels were detected using MitoSOX Red. Cells were incubated with MitoSOX Red working solution at 37 °C for 10 min in the dark, washed with PBS, and analyzed by flow cytometry.

Mitochondrial respiration assay

Mitochondrial oxidative phosphorylation capacity was assessed by measuring the oxygen consumption rate (OCR) using Seahorse XFe96

Extracellular Flux Analyzer (Agilent, CA, USA). Cells were seeded in Seahorse assay plates and subjected to the indicated treatments. Before analysis, cells were switched to Seahorse assay medium and equilibrated in a CO_2-free incubator. OCR was recorded under basal conditions and following sequential administration of oligomycin, FCCP, and rotenone/ antimycin A.

Co-immunoprecipitation (co-IP)

Protein lysates were prepared from plasmid-transfected HEK293T cells using RIPA buffer. For immunoprecipitation, lysates were incubated with the indicated antibodies and Protein A/G agarose beads (Beyotime) at 4 °C overnight. After extensive washing, the beads were boiled in loading buffer to release bound proteins. Immunoprecipitated proteins were subsequently detected by western blotting.

Immunohistochemistry

Tumor specimens were fixed with 10% neutral-buffered formalin, processed for paraffin embedding, and cut into 4 μm sections. Following deparaffinization and rehydration, antigen retrieval was performed using citrate buffer (pH 6.0). Sections were then blocked and incubated with primary antibodies at 4 °C overnight, followed by detection with HRP-labeled secondary antibodies. Signals were developed using a DAB chromogenic substrate, and hematoxylin was applied for nuclear counterstaining. Immunostaining results were assessed in randomly selected microscopic fields by evaluating staining intensity and the proportion of positive cells. Quantification was performed using ImageJ software or by manual counting, and data were presented as the percentage of positively stained cells.

Dephosphorylation assay

Purified Flag-tagged proteins, including Flag-PYCR2 and Flag-PP2Ac, were prepared and equal amounts of purified Flag-tagged proteins (5 μg) were incubated with lambda protein phosphatase (λPPase, 400 U) in phosphatase reaction buffer containing HEPES (20 mM, pH 7.4), DTT (1 mM), EDTA (1 mM), BSA (0.1 mg/mL), $MgCl_2$ (1 mM), and protease inhibitors. The reaction system was supplemented with Flag-eIF2α protein (3 μg) and incubated at 37 °C for 2 h. Following incubation, reactions were terminated by adding 5 × SDS loading buffer and heating to denature proteins, followed by SDS-PAGE and immunoblotting to assess the dephosphorylation status of eIF2α.

PP2A enzyme activity assay

PP2A activity was determined using a serine/threonine phosphatase assay kit (Promega) following the manufacturer's protocol. The assay is based on the dephosphorylation of a synthetic phosphopeptide substrate (RRA(p)TVA) and subsequent detection of released phosphate using a molybdate-malachite green reagent. For cell lysates, samples were desalted to remove free phosphate and small-molecule inhibitors prior to analysis, and equivalent amounts of protein were subjected to analysis. Briefly, reactions were carried out in a 50 μL volume at 37 °C for 1 h containing substrate, sample and reaction buffer. The reaction was terminated by adding molybdate dye reagent, and absorbance was measured at 600 nm using a microplate reader. Phosphate standards were used to generate a calibration curve, and PP2A enzymatic activity was calculated accordingly.

NAD^+/NADH and $NADP^+$/NADPH measurement

Intracellular NAD^+/NADH and $NADP^+$/ NADPH levels were determined using commercial colorimetric assay kits (Sangon Biotech) according to the manufacturer's protocols. Briefly, approximately 5×10^6 cells were harvested and extracted with acidic or alkaline extraction buffer, respectively. Cell suspensions were subjected to ultrasonic disruption on ice, boiled for 5 min, cooled, and centrifuged at 10000 g for 10 min at 4 °C. The supernatants were then neutralized with the corresponding opposite extraction buffer and centrifuged again, and the final supernatants were used for subsequent analysis. The reaction mixtures were prepared according to the kit protocol, incubated at room temperature in the dark, and the absorbance was measured at 570 nm using a microplate reader. The NAD^+/NADH and $NADP^+$/ NADPH ratios were calculated according to the measured concentrations, and the results were normalized to protein concentration or cell number as indicated.

Proline measurement assay

Proline levels were quantified using a colorimetric assay kit (Sangon Biotech) following the manufacturer's instructions. Cells were collected and lysed in extraction buffer, followed by heat treatment at 100 °C for 10 min. After centrifugation at 10000 g, the resulting supernatant was incubated with assay reagents to allow chromophore formation. Absorbance was recorded at 520 nm using a spectrophotometer. Proline concentrations were calculated from a standard curve and normalized to cell numbers.

SUnSET assay

Global protein synthesis was evaluated using the SUnSET assay. Briefly, cells were labeled with puromycin (5 μg/mL) for 2 h before harvest. Following lysis, incorporated puromycin was detected by western blotting with an anti-puromycin antibody as an indicator of nascent protein synthesis.

Phospho-protein array analysis

Human phosphorylation pathway profiling array (RayBiotech, C55) was performed according to the manufacturer's instructions. Briefly, equal amounts of protein lysates were incubated with array membranes after blocking, followed by incubation with detection antibody cocktail and HRP-conjugated secondary antibody. Signals were detected using chemiluminescence and quantified by densitometry. After background correction, signal intensities were normalized to the positive controls.

RNA sequencing and bioinformatic analysis

HCC3975 and HCC3975-R cells were analyzed in parallel, with three biological replicates in each group. RNA-seq experiments and downstream data analyses were conducted by LC-Bio Technologies (Hangzhou) Co., Ltd. Following normalization of raw counts, differential gene expression was assessed using the DESeq2 R package. Genes meeting the criteria of $|\log2FC| \geq 1$ and $P < 0.05$ were defined as significantly differentially expressed.

Proteomic mass spectrometry analysis

Protein bands obtained from SDS-PAGE were excised and subjected to digestion. Briefly, the gel pieces were destained, reduced with dithiothreitol, alkylated with iodoacetamide, and subsequently digested with trypsin at 37 °C overnight. The extracted peptides were extracted and analyzed by LC-MS/MS. Raw mass spectrometry data were processed using MaxQuant, and peptide/protein identification was performed with FDR < 1%. Identified candidate proteins were further analyzed and validated by co-immunoprecipitation assays.

Untargeted metabolomics analysis

Untargeted metabolomics analysis was performed by LC-Bio Technology Co., Ltd. (Hangzhou, China). Metabolites were extracted from cells with 80% methanol and analyzed by UPLC-MS/MS. Raw data were processed using XCMS and metaX for peak alignment, metabolite identification, and statistical analysis. Differential metabolites were identified using the criteria of $P < 0.05$, fold change > 1.2, and VIP ≥ 1.

Statistical analysis

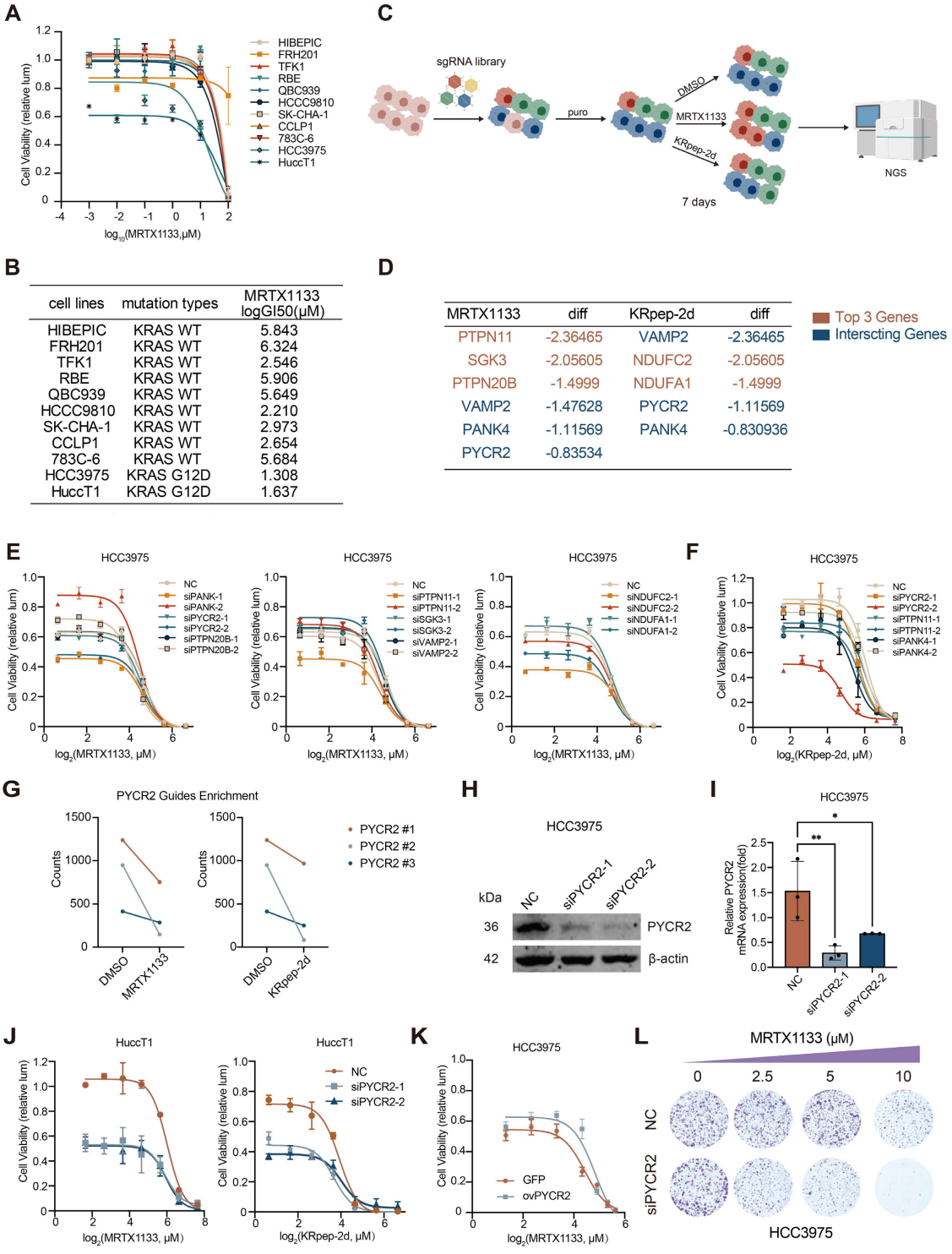
All statistical analyses were conducted using GraphPad Prism 9. Quantitative data are presented as mean ± SD. Comparisons between two groups were performed using unpaired two-tailed Student's t-test, Welch's unpaired two-tailed t-test or the Mann-Whitney U test, as appropriate based on data distribution. For comparisons among multiple groups, one-way ANOVA followed by suitable post hoc multiple comparison tests was applied. The relationship between PYCR2 expression and overall survival in the public CCA cohort (FU-iCCA cohort) was assessed using Kaplan-Meier analysis with the log-rank test [15]. $P < 0.05$ was considered statistically significant, and ns denotes a non-significant difference.

Results

CRISPR screening identifies PYCR2 as a key regulator of MRTX1133 sensitivity in *KRAS*^{G12D} CCA

To identify potential targets that enhance sensitivity to MRTX1133, we first performed a drug sensitivity profiling across a panel of 11 CCA cell lines and found that MRTX1133 preferentially inhibited the proliferation of *KRAS*^{G12D}-mutant cells (Fig. 1A-B). Based on these results, HCC3975 and HuCCT1 cells were selected for subsequent mechanistic studies. To systematically identify determinants of drug response, we performed a CRISPR-Cas9 loss-of-function screen targeting 2333 druggable kinase-related genes in HCC3975 cells under selective pressure with either MRTX1133 or KRpep-2d (Fig. 1C). KRpep-2d, a *KRAS*^{G12D}-selective inhibitory peptide, was used as a complementary *KRAS*^{G12D}-targeting agent in the screen [16]. Candidate genes for further validation were selected based on the top three overlapping hits between the two screens together with the top three ranked genes in each treatment group, yielding eight non-redundant candidates (Fig. 1D). Validation experiments assessing the effects of these candidates on MRTX1133 sensitivity revealed that PYCR2, PTPN11 and PANK4 exhibited notable sensitizing effects (Fig. 1E). Further validation using KRpep-2d treatment confirmed that PYCR2 conferred the most robust sensitization phenotype (Fig. 1F). Depletion of multiple independent PYCR2-targeting sgRNAs under both treatment conditions further supports its role as a key sensitizer (Fig. 1G). Efficient knockdown of PYCR2 was confirmed by qPCR and immunoblotting (Fig. 1H-I). Consistently, PYCR2 depletion also significantly increased sensitivity to MRTX1133 and KRpep-2d in HuCCT1 cells (Fig. 1J).

Conversely, overexpression of PYCR2 significantly reduced the sensitivity of HCC3975 cells to MRTX1133, further supporting PYCR2 induces resistance to *KRAS*^{G12D}-targeted therapy (Fig. 1K). Finally, functional validation further demonstrated that depletion of PYCR2 markedly enhanced the efficacy of MRTX1133, as evidenced by reduced clonogenic growth (Fig. 1L).



cell lines	mutation types	MRTX1133 logGI50(μM)
HIBEPIC	KRAS WT	5.843
FRH201	KRAS WT	6.324
TFK1	KRAS WT	2.546
RBE	KRAS WT	5.906
QBC939	KRAS WT	5.649
HCCC9810	KRAS WT	2.210
SK-CHA-1	KRAS WT	2.973
CCLP1	KRAS WT	2.654
783C-6	KRAS WT	5.684
HCC3975	KRAS G12D	1.308
HuccT1	KRAS G12D	1.637

MRTX1133	diff	KRpep-2d	diff
PTPN11	-2.36465	VAMP2	-2.36465
SGK3	-2.05605	NDUFC2	-2.05605
PTPN20B	-1.4999	NDUFA1	-1.4999
VAMP2	-1.47628	PYCR2	-1.11569
PANK4	-1.11569	PANK4	-0.830936
PYCR2	-0.83534		

Figure 1. CRISPR screening identifies PYCR2 as an important sensitizer of MRTX1133 response in CCA. (A) Drug sensitivity profiling of CCA cell lines treated with MRTX1133. (B) *KRAS* mutation status in 11 CCA cell lines. (C) Schematic overview of the CRISPR-Cas9 loss-of-function screen under MRTX1133 or KRpep-2d selection, created by BioGDP.com. (D) Candidate genes identified based on overlapping top hits and integrated ranking. (E-F) Drug sensitivity assays in HCC3975 cells after knockdown of candidate genes under MRTX1133 (E) or KRpep-2d (F). (G) Depletion of sgRNAs targeting PYCR2 in both screening conditions. (H-I) Validation of PYCR2 knockdown by immunoblotting (H) and qPCR (I) (n = 3 biological replicates, one-way ANOVA). (J) Drug sensitivity assays following PYCR2 knockdown in HuCCT1 cells treated with MRTX1133 and KRpep-2d. (K) Drug sensitivity assays following PYCR2 overexpression under MRTX1133 treatment. (L) Representative images of colony formation in control and PYCR2-depleted HCC3975 cells treated with MRTX1133. Values are expressed as mean ± SD, *$P < 0.05$, **$P < 0.01$. Calculated GI_{50} values are summarized in Supplementary Table S3.

PYCR2 expression is significantly elevated in MRTX1133-resistant cells

To explore the molecular mechanisms underlying acquired resistance to MRTX1133, we established a MRTX1133-resistant CCA cell line (HCC3975-R) from the parental HCC3975 cells via stepwise exposure to escalating concentrations of the drug (Fig. 2A-B). Drug sensitivity assays showed that HCC3975-R cells maintained higher viability than parental cells at the same MRTX1133 concentrations, supporting the successful establishment of the MRTX1133-resistant cell line. Transcriptomic profiling revealed a significant upregulation of the MAPK signaling pathway in resistant cells (Fig. 2C). This was supported by higher levels of p-ERK detected by immunoblotting (Fig. 2D). In line with this aberrant pathway activation, the resistant cells required substantially higher concentrations of MRTX1133 to suppress ERK phosphorylation, indicative of impaired drug sensitivity compared with the parental cells (Fig. 2E).

Further analysis identified PYCR2 as one of the most significantly upregulated genes in resistant cells, which was subsequently validated at both the mRNA and protein levels (Fig. 2F-H). Functionally, knockdown of PYCR2 in HCC3975-R cells restored sensitivity to MRTX1133 (Fig. 2I). Specifically, PYCR2 knockdown led to enhanced growth inhibition and a marked reduction in clonogenic capacity of resistant cells upon MRTX1133 treatment (Fig. 2J). To further evaluate the clinical relevance of PYCR2 in cholangiocarcinoma, we analyzed a public CCA cohort (FU-iCCA cohort) [15]. Kaplan-Meier analysis demonstrated no significant association between PYCR2 expression and overall survival (Supplementary Fig. S1A). Likewise, no significant association was observed between PYCR2 expression and *KRAS* mutation status or tumor stage (Supplementary Fig. S1B-C).

Taken together, our data indicate that PYCR2 plays a critical role in mediating acquired resistance to MRTX1133 and that targeting PYCR2 represents a potential strategy to resensitize drug-resistant CCA cells to $KRAS^{G12D}$ inhibitor.

PYCR2 depletion increases MRTX1133-induced apoptosis and suppresses tumor growth under MRTX1133 treatment

Having identified PYCR2 as a candidate regulator of MRTX1133 sensitivity, we next investigated its functional role in modulating cell survival and tumor growth. Flow cytometry analysis revealed a clear increase in the proportion of apoptotic cells following PYCR2 knockdown under MRTX1133 treatment (Fig. 3A). Cell cycle analysis further showed a more pronounced cell cycle arrest (Fig. 3B). Consistent with these *in vitro* observations, *in vivo* xenograft studies demonstrated that either PYCR2 depletion or MRTX1133 treatment alone suppressed tumor growth. Notably, the combination of both interventions elicited a markedly more potent antitumor effect (Fig. 3C-D). Throughout the experiment, body weights remained stable across all groups, suggesting the treatment was well tolerated (Fig. 3E). In line with these findings, tumors from the combination group showed reduced Ki67 and PCNA staining, indicating lower proliferative capacity (Fig. 3F). Collectively, these results substantiate PYCR2 as an important factor that governs the response to MRTX1133 in CCA.

PYCR2 regulates MRTX1133 response independently of its canonical metabolic enzymatic function

Given that PYCR2 is located in the mitochondria and catalyzes the NADH-dependent conversion of pyrroline-5-carboxylate (P5C) to proline during proline biosynthesis (Fig. 4A), we first investigated whether its role in regulating MRTX1133 sensitivity depends on its canonical metabolic function or affects mitochondrial and redox homeostasis [17, 18].

Untargeted metabolomic analysis showed that representative metabolites involved in proline and NAD metabolism exhibited limited overall alterations following PYCR2 depletion (Fig. 4B). Further quantitative analysis revealed a modest but significant decrease in proline levels (Fig. 4C), whereas glutamate levels remained unchanged (Fig. 4D). These findings suggest that PYCR2 depletion reduces intracellular proline abundance without broadly remodeling proline- or NAD-related metabolism. Consistent with these findings, intracellular NAD^+/NADH and $NADP^+$/NADPH ratios were not significantly affected by PYCR2 knockdown (Fig. 4E). Furthermore, neither total intracellular ROS nor mitochondrial ROS levels, as assessed by DCFH-DA and MitoSOX staining respectively, were significantly affected by PYCR2 knockdown (Fig. 4F-G). Consistent with these findings, Seahorse analysis demonstrated that PYCR2 depletion did not significantly alter mitochondrial respiratory function, including basal respiration, ATP production, maximal respiration, or spare respiratory capacity (Fig. 4H).

To determine whether these metabolic changes contribute to MRTX1133 resistance, we next performed metabolite supplementation assays. Exogenous supplementation with glutamate, P5C, or proline failed to rescue the increased sensitivity to

MRTX1133 induced by PYCR2 knockdown (Fig. 4I-L). Consistently, pharmacological modulation of NAD metabolism using nicotinamide (NAM), a precursor that replenishes intracellular NAD^+ via the salvage pathway, or FK866, a NAMPT inhibitor that blocks NAD^+ biosynthesis, did not affect cellular sensitivity to MRTX1133 (Fig. 4M). Collectively, these results suggest that the role of PYCR2 in regulating MRTX1133 sensitivity is independent of its canonical enzymatic function in proline metabolism.

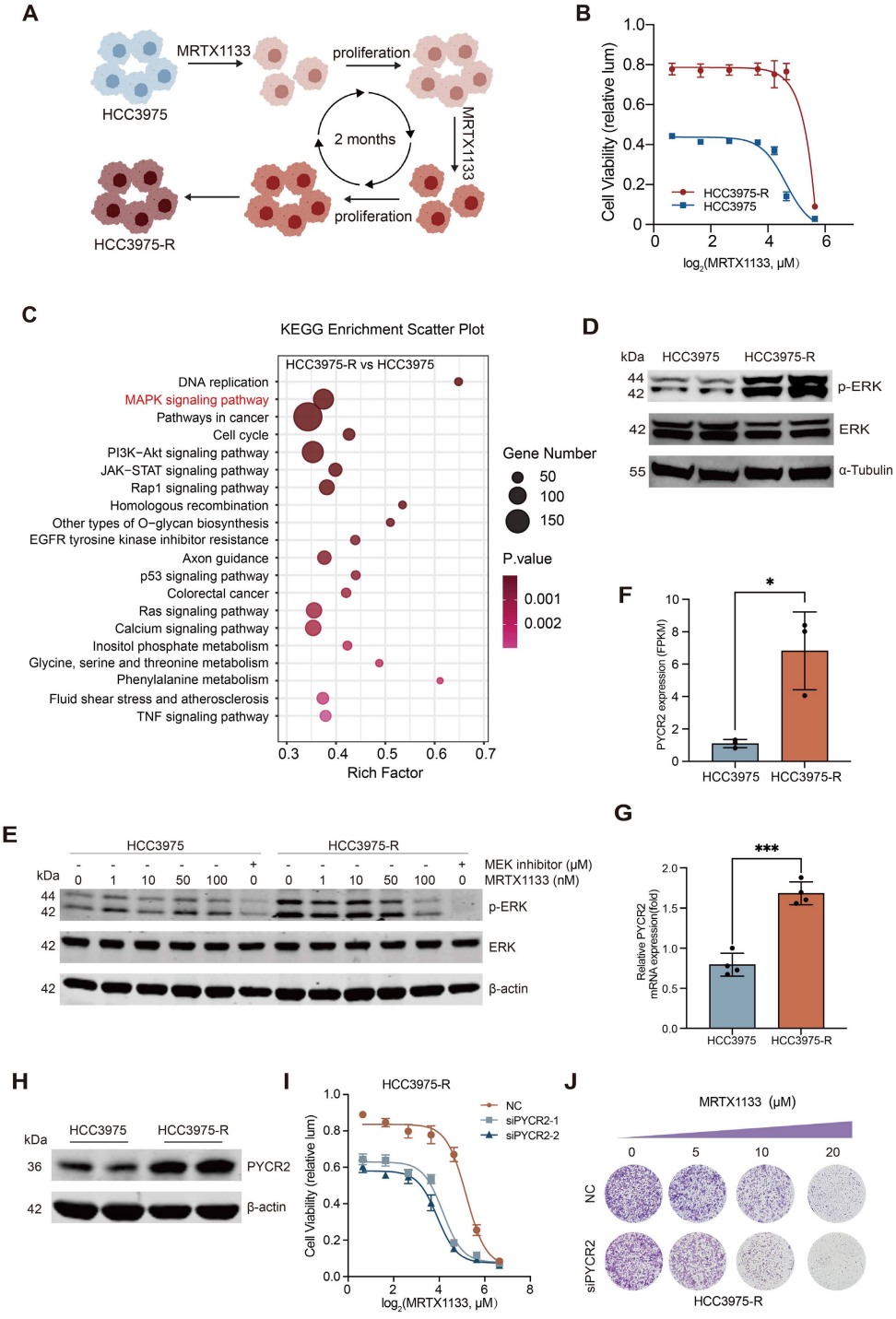


Figure 2. PYCR2 is associated with acquired resistance to MRTX1133 in CCA. (A) Schematic illustration of the establishment of MRTX1133-resistant HCC3975 cells, created by BioGDP.com. (B) Drug sensitivity assays of HCC3975 and HCC3975-R cells treated with MRTX1133. (C) KEGG pathway analysis comparing HCC3975 and HCC3975-R cells. (D) Immunoblot analysis of p-ERK and total ERK levels in HCC3975 and HCC3975-R cells. (E) Immunoblot analysis of p-ERK and total ERK levels in HCC3975 and HCC3975-R cells treated with increasing concentrations of MRTX1133. (F) Transcriptomic analysis showing PYCR2 mRNA expression levels in HCC3975 and HCC3975-R cells (n = 3 biological replicates, Welch's unpaired two-tailed t-test). (G) PYCR2 expression by qPCR (n = 3 biological replicates, unpaired two-tailed Student's t-test). (H) PYCR2 expression by immunoblotting. (I) Drug sensitivity assays of HCC3975-R cells following PYCR2 knockdown under MRTX1133 treatment. (J) Colony formation assays of HCC3975-R cells with or without PYCR2 knockdown under MRTX1133 treatment. Values are expressed as mean ± SD, $^*P < 0.05$, $^{***}P < 0.001$. Calculated GI_{50} values are summarized in Supplementary Table S3.

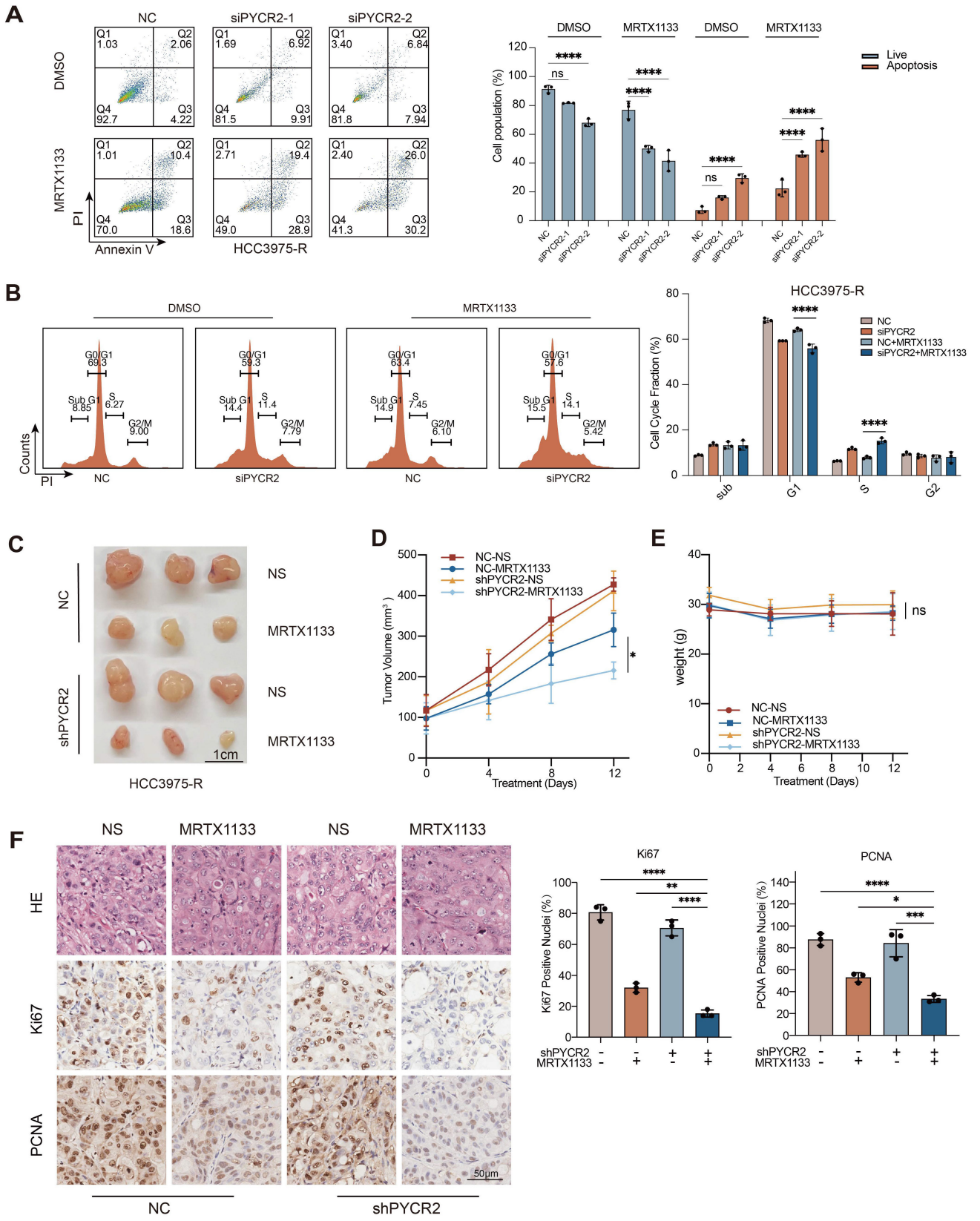


Figure 3. Loss of PYCR2 enhances MRTX1133-induced apoptosis and inhibits tumor growth. (A) Representative dot plots and quantification of flow cytometry analysis of apoptosis in control and PYCR2-depleted cells under MRTX1133 treatment (20 μM) (n = 3 biological replicates, one-way ANOVA). (B) Representative histograms and quantification of cell cycle in control and PYCR2-depleted cells under MRTX1133 treatment (20 μM) (n = 3 biological replicates, one-way ANOVA). (C) Subcutaneous xenograft tumors derived from control or shPYCR2 HCC3975-R cells treated with vehicle (n = 3) or MRTX1133 (10 mg/kg, n = 3). (D) Tumor growth curves of xenografts under the treatment (n = 3 biological replicates, two-way ANOVA). (E) Body weight curves of mice during the treatment (n = 3 biological replicates, two-way ANOVA). (F) Representative immunohistochemical staining of Ki67 and PCNA in tumor sections and corresponding quantification (n = 3 biological replicates, one-way ANOVA). Values are expressed as mean ± SD, ns: not significant, *$P < 0.05$, **$P < 0.01$, ***$P < 0.001$, ****$P < 0.0001$.

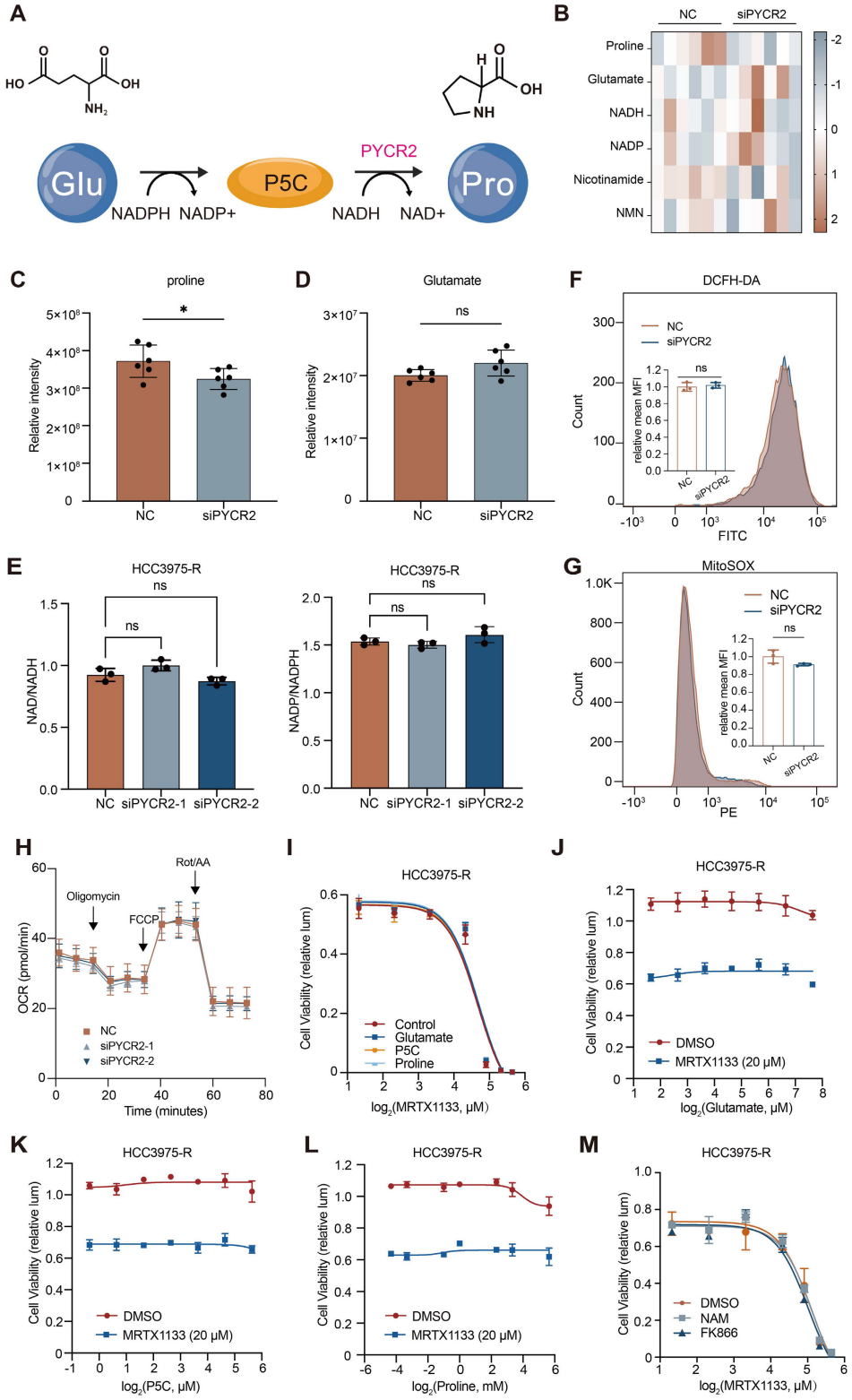


Figure 4. PYCR2 regulates MRTX1133 sensitivity independently of its canonical role in proline metabolism. (A) Schematic illustration of PYCR2 function in the proline metabolic pathway, created by BioGDP.com. (B) Heatmap of representative metabolites associated with proline and NAD metabolism in NC and PYCR2-depleted HCC3975-R cells. Data are presented as row Z-score-normalized metabolite abundance. (C-D) Relative abundances of proline(C) and glutamate(D) in NC and PYCR2-depleted HCC3975-R cells, as determined by untargeted metabolomic analysis (n = 6 biological replicates, unpaired two-tailed Student's t-test). (E) Measurement of intracellular NAD^+/NADH and $NADP^+$/NADPH levels in control and PYCR2-depleted cells under MRTX1133 treatment (20 μM) (n = 3 biological replicates, one-way ANOVA). (F-G) Representative flow cytometry histograms of DCFH-DA(F) and MitoSOX(G) staining in NC and PYCR2-silenced cells under MRTX1133 treatment (20 μM) (n = 3 biological replicates, Welch's unpaired two-tailed t-test). (H) Seahorse analysis of mitochondrial respiration in control and PYCR2-silenced cells under MRTX1133 treatment (20 μM). (I) Cell viability assays following supplementation with glutamate (20 μM), P5C (20 μM), or proline (1 mM) in PYCR2-depleted cells under MRTX1133 treatment. (J-L) Cell viability assays with increasing concentrations of glutamate(J), P5C(K), or proline(L) under MRTX1133 treatment (20 μM). (M) Drug sensitivity assays following treatment with NAM (5 mM) or FK866 (50 nM) in combination with MRTX1133. Values are expressed as mean ± SD, ns: not significant, $P < 0.05$. Calculated GI_{50} values are summarized in Supplementary Table S3.

PYCR2 modulates MRTX1133 sensitivity via regulation of eIF2α phosphorylation

To identify signaling pathways involved in PYCR2-mediated regulation of MRTX1133 sensitivity, we performed a phospho-protein array analysis. Knockdown of PYCR2 under MRTX1133 treatment led to increased phosphorylation levels of both eIF2α and ATM (Fig. 5A). Subsequent immunoblot analysis showed that only p-eIF2α was stably elevated, whereas changes in p-ATM were not reproducible. This suggests that eIF2α is likely the main downstream target (Fig. 5B).

In line with this, PYCR2 overexpression reduced eIF2α phosphorylation and increased ERK activation, supporting the role of PYCR2 in regulating eIF2α phosphorylation and MAPK signaling (Fig.5C). Functionally, reducing eIF2α levels enhanced cellular sensitivity to MRTX1133 (Fig.5D). In parallel, pharmacological inhibition of eIF2α dephosphorylation using salubrinal similarly enhanced the response to MRTX1133 (Fig. 5E). Notably, overexpression of eIF2α reversed the heightened drug sensitivity triggered by PYCR2 silencing (Fig. 5F). Consistently, colony formation assays demonstrated that restoration of eIF2α expression significantly rescued the impaired clonogenic growth caused by PYCR2 depletion under MRTX1133 treatment (Fig. 5G), further supporting that PYCR2 regulates drug response through eIF2α phosphorylation. Mechanistically, PYCR2 depletion markedly suppressed global protein translation, as determined by the SUnSET assay (Fig. 5H). Taken together, these data identify eIF2α phosphorylation as an important downstream mediator of PYCR2 in regulating cellular sensitivity to MRTX1133.

PYCR2 promotes eIF2α dephosphorylation via PP2Ac

To further elucidate how PYCR2 regulates eIF2α phosphorylation, we first examined whether the two proteins interact directly. Co-IP assays in HCC3975-R cells showed a physical association between PYCR2 and eIF2α (Fig. 6A-B). However, *in vitro* phosphatase assays indicated that PYCR2 does not directly dephosphorylate eIF2α, suggesting the involvement of an intermediary phosphatase (Fig. 6C-D). To identify the phosphatase potentially involved in PYCR2-mediated eIF2α dephosphorylation, we performed IP-MS analyses using both PYCR2 and eIF2α as bait proteins and focused on proteins shared by the two interactomes. The overlapping proteins are listed in Supplementary Table S2. Among these candidates, PP2A (PPP2CA/PPP2CB) and PP1 (PPP1CA/PPP1CB/PPP1CC) were identified as potential phosphatases. Co-immunoprecipitation assays showed that PPP1CC did not interact with eIF2α (Supplementary Fig. S2A), whereas PP2Ac associated with both PYCR2 and eIF2α (Fig. 6F). Furthermore, confocal immunofluorescence staining demonstrated clear subcellular co-localization of PP2Ac with eIF2α and PYCR2 (Fig. 6G).

Functionally, pharmacological inhibition of PP2Ac activity using either LB100 or okadaic acid increased eIF2α phosphorylation (Fig. 6H-I and Supplementary Fig. S2B). Moreover, combined treatment with okadaic acid and MRTX1133 significantly enhanced the anti-proliferative effect of MRTX1133, indicating that inhibition of PP2Ac sensitizes cholangiocarcinoma cells to $KRAS^{G12D}$-targeted therapy (Fig. 6J). Similarly, genetic silencing of PP2Ac elevated p-eIF2α levels (Fig. 6K and Supplementary Fig. S2C) and increased cellular sensitivity to MRTX1133 (Fig. 6L). Consistent with these findings, PP2A phosphatase activity was significantly decreased following PYCR2 knockdown (Fig. 6M), further supporting a role for PYCR2 in modulating PP2A activity. Collectively, these findings suggest that PYCR2 facilitates eIF2α dephosphorylation in a PP2Ac-dependent manner.

Inhibition of eIF2α dephosphorylation enhances the antitumor efficacy of MRTX1133 *in vivo*

To evaluate the therapeutic potential of targeting eIF2α signaling *in vivo*, we established a syngeneic subcutaneous cholangiocarcinoma model by implanting the murine primary CCA cell line KPT8 into immunocompetent C57BL/6 mice. Tumor-bearing mice were treated with MRTX1133 alone, the eIF2α dephosphorylation inhibitor salubrinal alone, or a combination of both agents for two consecutive weeks. Each single treatment produced a moderate reduction in tumor growth. In contrast, the combination led to a much stronger suppression of tumor progression, indicating a synergistic antitumor effect (Fig. 7A-B). Notably, no significant changes in body weight were observed across all groups, suggesting a good tolerability and negligible systemic toxicity (Fig. 7C). Further immunohistochemical analysis of tumor tissues revealed diminished expression of cellular proliferation markers in the combination treatment group, corroborating the enhanced antitumor activity (Fig. 7D). Likewise, combined treatment with salubrinal and MRTX1133 markedly increased p-eIF2α staining while further suppressing p-ERK, supporting effective inhibition of the PYCR2-PP2Ac-eIF2α signaling axis *in vivo* (Fig. 7D). Immunohistochemical staining for CD8 showed

no significant differences in intratumoral CD8⁺ T-cell infiltration among the treatment groups (Fig. 7D), suggesting that the enhanced therapeutic efficacy was not associated with CD8⁺ T-cell infiltration. Together, these results demonstrate that blocking eIF2α dephosphorylation can improve the *in vivo* response to MRTX1133, highlighting a promising combinatorial therapeutic strategy for *KRAS*^{G12D}-driven CCA (Fig. 7E).

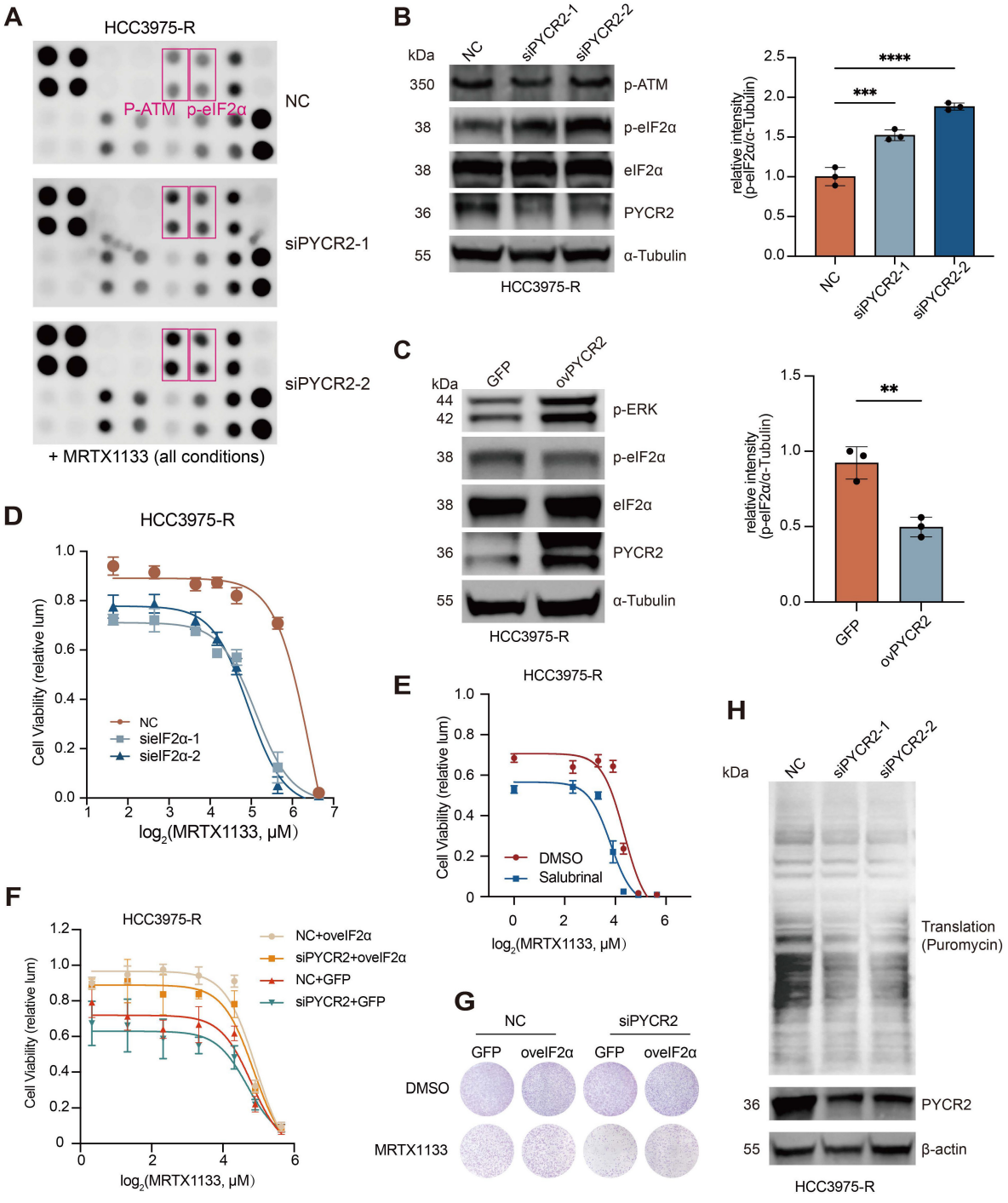


Figure 5. PYCR2 regulates MRTX1133 response through eIF2α phosphorylation and protein translational control. (A) Phospho-protein array analysis in control and PYCR2-depleted cells under MRTX1133 treatment (20 μM). (B) Immunoblot validation of p-eIF2α and p-ATM levels following PYCR2 knockdown under MRTX1133 treatment (20 μM) and corresponding quantification (n = 3 biological replicates, one-way ANOVA). (C) Immunoblot analysis of p-eIF2α following PYCR2 overexpression under MRTX1133 treatment (20 μM) and corresponding quantification (n = 3 biological replicates, Welch's unpaired two-tailed t-test). (D) Drug sensitivity assays following eIF2α knockdown under MRTX1133 treatment. (E) Drug sensitivity assays of MRTX1133 treated with or without salubrinal. (F) Drug sensitivity assays in PYCR2-depleted cells with or without eIF2α overexpression under MRTX1133 treatment. (G) Representative images of colony formation assays in PYCR2-depleted cells with or without eIF2α overexpression under MRTX1133 treatment (20 μM). (H) SUnSET assay measuring global protein synthesis following PYCR2 knockdown. Values are expressed as mean ± SD, $^{**}P < 0.01$, $^{***}P < 0.001$, $^{****}P < 0.0001$.

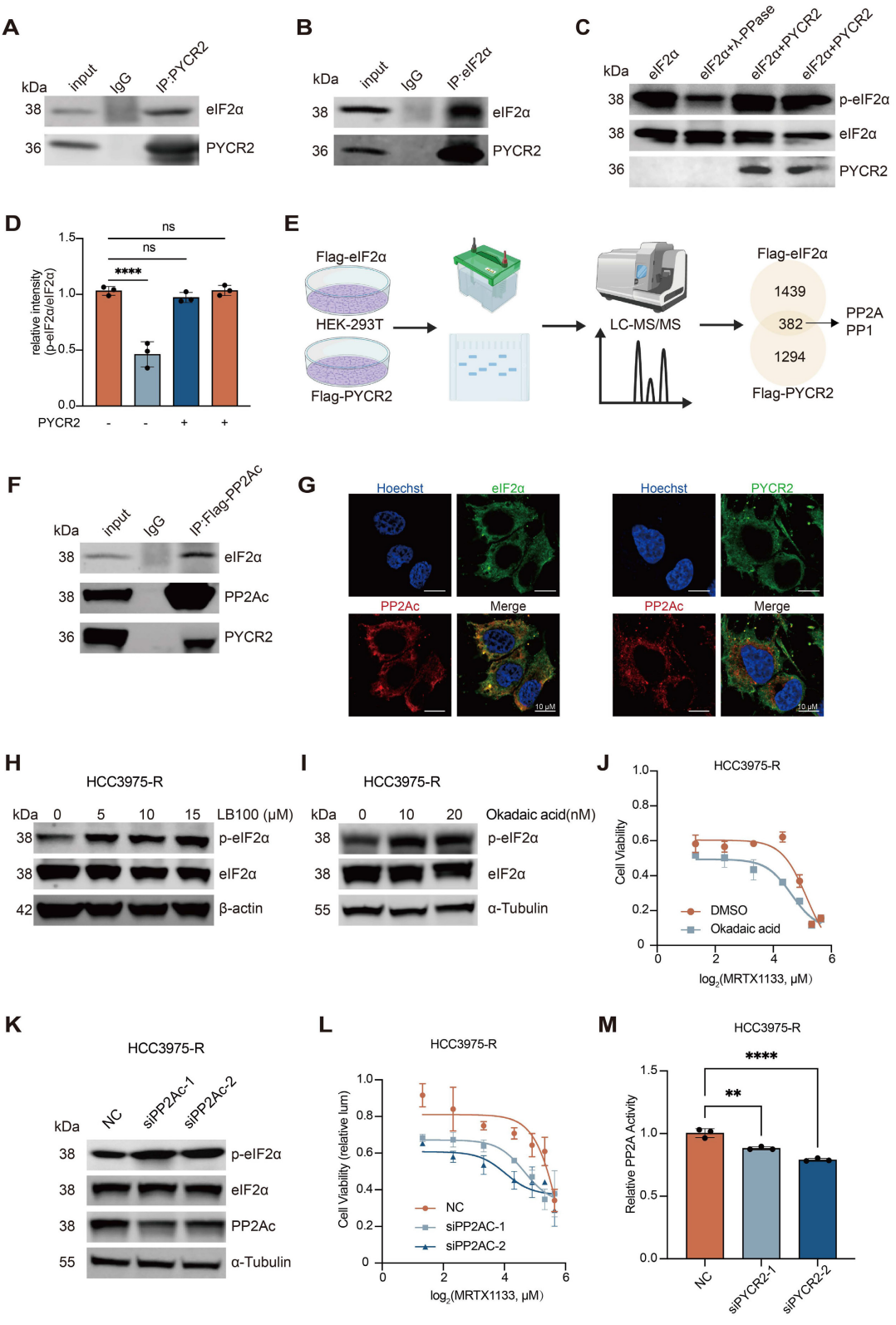


Figure 6. PYCR2 promotes eIF2α dephosphorylation through a PP2Ac-dependent mechanism. (A-B) Co-IP assays in HCC3975-R cells showing the interaction between PYCR2 and eIF2α. (C-D) *In vitro* phosphatase assay assessing the effect of PYCR2 on eIF2α phosphorylation (C) with corresponding quantification (D) (n = 3 biological replicates, one-way ANOVA). (E) Mass spectrometry analysis identifying PP2Ac as a common interacting protein of PYCR2 and eIF2α, created by BioGDP.com. (F) Co-IP assays showing the interaction among PYCR2, eIF2α, and PP2Ac in HCC3975-R cells. (G) Representative confocal immunofluorescence images showing the subcellular co-localization of PP2Ac with eIF2α and PP2Ac with PYCR2 in HCC3975-R cells. Scale bars, 10 μm. (H-I) Immunoblot analysis of p-eIF2α and total eIF2α in HCC3975-R cells treated with the PP2A inhibitors LB100 (H) or Okadaic acid (I) for 24 h. (J) Cell viability assay of HCC3975-R cells treated with MRTX1133 alone or in combination with okadaic acid (5 nM). (K) Immunoblot analysis of p-eIF2α and total eIF2α following PP2Ac knockdown or NC. (L) Cell viability assay of control and PP2Ac-silenced HCC3975-R cells treated with the indicated concentrations of MRTX1133. (M) PP2A enzymatic activity in HCC3975-R cells following PYCR2 knockdown or NC under MRTX1133 treatment (20 μM) (n = 3 biological replicates, one-way ANOVA). Values are expressed as mean ± SD, $^{**}P < 0.01$, $^{****}P < 0.0001$, ns: not significant.

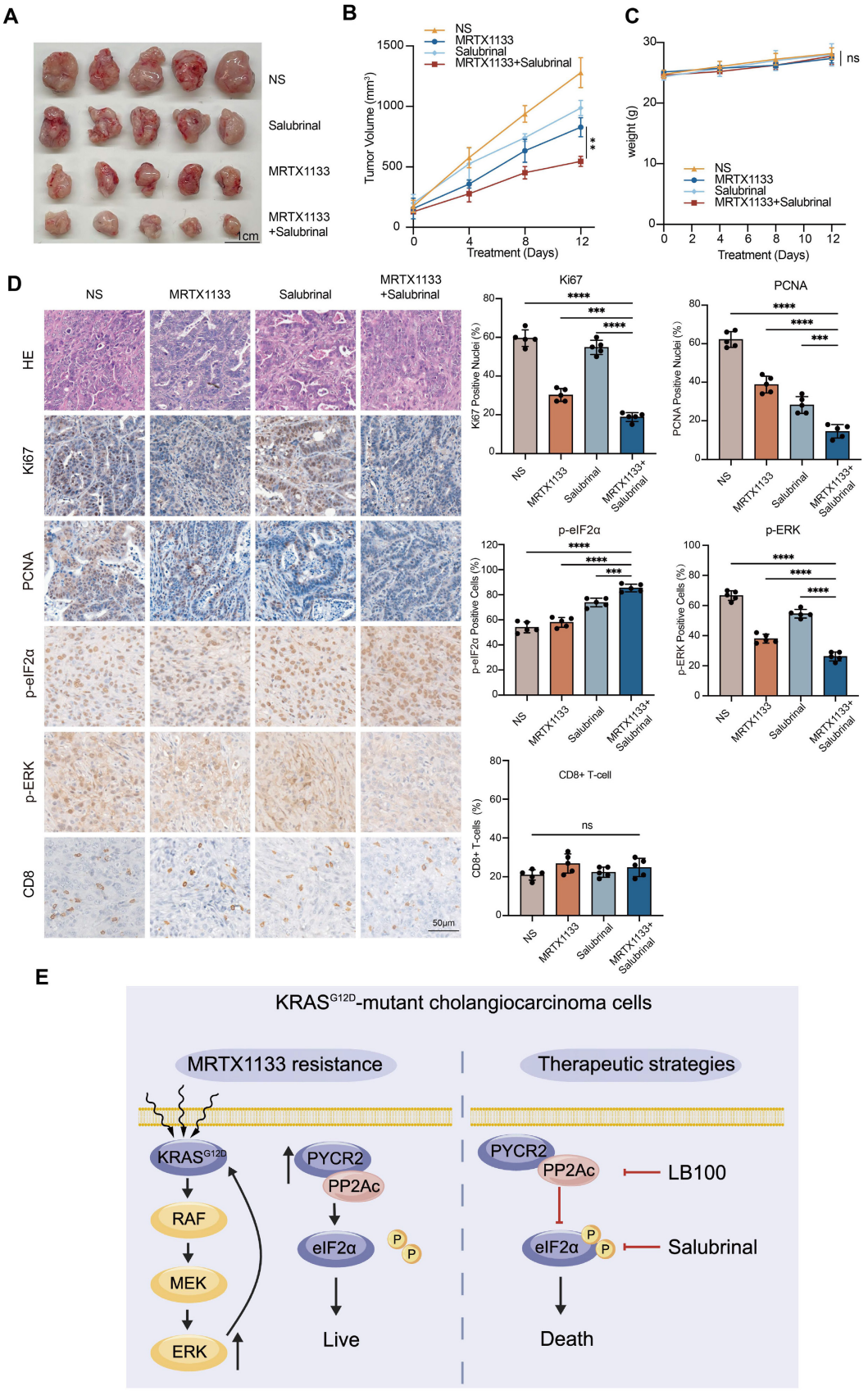


Figure 7. Combination MRTX1133 and salubrinal treatment *in vivo*. (A) Representative images of KPT8-derived xenograft tumors under the indicated treatments. (B) Tumor growth curves during the treatment period (n = 5 biological replicates, two-way ANOVA). (C) Body weight measured throughout the treatment (n = 5 biological replicates, two-way ANOVA). (D) Representative immunohistochemical staining of Ki67, PCNA, p-eIF2α, p-ERK and CD8 with corresponding quantification (n = 5 biological replicates, one-way ANOVA). (E) Schematic illustration of the therapeutic strategy targeting eIF2α dephosphorylation in combination with MRTX1133, created by BioGDP.com. Values are expressed as mean ± SD, ***$P < 0.001$, ****$P < 0.0001$, ns: not significant.

Discussion

Recent advances in *KRAS*-targeted therapies have spurred intensive research on selective inhibition of $KRAS^{G12D}$ in cancer. The development of MRTX1133 and analogous compounds has opened new avenues for treating tumors driven by $KRAS^{G12D}$ [6]. However, intrinsic and acquired drug resistance remains a major barrier to durable therapeutic efficacy [7]. Here, we identify PYCR2 as a critical factor of MRTX1133 sensitivity in CCA. Notably, the regulatory role of PYCR2 in drug response is independent of its canonical metabolic function in proline biosynthesis. Instead, we uncover a nonmetabolic function of PYCR2 in association with eIF2α and facilitating its dephosphorylation through a PP2Ac-dependent mechanism, thereby sustaining global protein synthesis and promoting tumor cell survival under $KRAS^{G12D}$ inhibition. Targeting this axis significantly potentiates the antitumor activity of MRTX1133 both *in vitro* and *in vivo*, highlighting PYCR2 as a promising therapeutic target to overcome resistance to $KRAS^{G12D}$ inhibition in CCA.

Previous studies have linked *KRAS* inhibitor resistance to downstream pathway reactivation, epithelial-to-mesenchymal transition, and lineage plasticity [7-9]. Our findings expand this mechanistic landscape by demonstrating that PYCR2-mediated translational control also contributes to therapeutic resistance, likely cooperating with MAPK reactivation to maintain tumor cell viability under therapeutic pressure. In this context, PYCR2 appears to influence not only the immediate response to treatment but also longer-term adaptive resistance. Interestingly, although HCC3975-R cells exhibited marked resistance to MRTX1133 *in vitro*, MRTX1133 still retained partial antitumor activity in the xenograft model. This discrepancy likely reflects the greater complexity of the *in vivo* tumor environment, where factors such as limited drug exposure heterogeneity, stromal interactions, and metabolic constraints may influence therapeutic responses.

PYCR2, a key enzyme in proline biosynthesis, catalyzes the conversion of P5C to proline [18]. Mounting evidence indicates that metabolic enzymes exert noncanonical functions beyond metabolic regulation [10, 11, 19]. Kuo *et al*. demonstrated that PYCR2 physically interacts with RRM2B and cooperates in protecting cells against oxidative stress, highlighting a role for PYCR2 in cellular stress responses through protein-protein interactions rather than solely through metabolic regulation [20]. More recently, Tamang *et al*. reported that PYCR2 promotes colorectal carcinogenesis by regulating the MASTL/Wnt/β-catenin signaling pathway, further supporting its role as a signaling regulator beyond proline metabolism [21]. Here, we uncover a previously unrecognized non-metabolic role of PYCR2 in regulating therapeutic response. PYCR2 functions as an adaptive regulator that links oncogenic stress responses to translational control via modulation of EIF2α phosphorylation. Given the established role of dysregulated eIF2α signaling in tumor progression and therapeutic resistance across multiple cancer types [22-27], our findings extend these observations by identifying PYCR2 as a previously unrecognized regulator of eIF2α phosphorylation.

Mechanistically, our study identifies PP2Ac as a critical intermediary linking PYCR2 to eIF2α regulation. The *in vitro* dephosphorylation assays indicate that PYCR2 itself does not directly catalyze eIF2α dephosphorylation. Instead, PYCR2 forms a complex with eIF2α and PP2Ac, thereby facilitating PP2Ac-dependent dephosphorylation of eIF2α. As a major serine/threonine phosphatase, PP2Ac governs a wide array of cellular processes including protein synthesis, cell cycle progression, proliferation, differentiation, and apoptosis [28, 29]. Our findings establish PYCR2 as a scaffold-like regulator that stabilizes the PP2Ac-eIF2α interaction, maintaining eIF2α in a hypophosphorylated state to sustain global protein synthesis under therapeutic stress.

Our work supports the therapeutic potential of targeting eIF2α phosphorylation to augment $KRAS^{G12D}$-targeted therapy. Inhibition of eIF2α dephosphorylation has been shown to reduce cancer cell viability and synergize with conventional anticancer agents across multiple tumor types [30]. Consistent with these observations, we found that Salubrinal, an inhibitor of eIF2α dephosphorylation, enhanced the antitumor efficacy of MRTX1133 in immunocompetent C57BL/6 mice without obvious systemic toxicity. Nevertheless, as with many targeted therapeutic strategies, prolonged inhibition of the PYCR2-PP2Ac-eIF2α axis may eventually trigger compensatory signaling events. Previous studies have shown that reactivation of the MAPK pathway, mTOR pathway and other stress-response networks represent common adaptive mechanisms underlying resistance to targeted therapies [31-33]. Although these potential compensatory pathways were beyond the scope of the present study, future investigations using long-term treatment models will be important to determine whether adaptive resistance emerges following sustained inhibition of the PYCR2-PP2Ac-eIF2α axis and to facilitate the development of more durable therapeutic strategies.

Several limitations should be considered. First, the structural basis of the PYCR2-PP2Ac-eIF2α interaction remains unclear, and further studies are

needed to elucidate whether PYCR2 directly stabilizes the phosphatase-substrate complex or acts indirectly. Second, other stress-related pathways may participate in PYCR2-mediated drug resistance and warrant further investigation. Third, our study focuses on CCA models, and whether this mechanism is conserved in other *KRAS*^{G12D} -driven cancers remains to be verified. Fourth, our *in vivo* studies were performed using subcutaneous xenograft models, which, although widely used for therapeutic evaluation, cannot fully reproduce the complex biliary tumor microenvironment or metastatic behavior of cholangiocarcinoma. Future studies using orthotopic transplantation models and genetically engineered mouse models will be important to further assess the therapeutic efficacy and mechanism of targeting the PYCR2-PP2Ac-eIF2α axis in a more physiologically relevant setting. Fifth, the HCC3975-R model was established through long-term exposure to progressively increasing doses of MRTX1133 and therefore represents a model of acquired resistance following *KRAS*^{G12D} inhibition. The selective pressure imposed by this procedure may enrich specific cellular adaptations and partly account for the relatively high drug concentrations used in some assays. Thus, this model may not fully recapitulate the heterogeneous resistance mechanisms arising in patients. Nevertheless, the identification of PYCR2 in this model suggests that the PYCR2-PP2Ac-eIF2α axis may be particularly relevant to acquired resistance emerging after *KRAS*^{G12D}-targeted treatment and may provide a potential therapeutic vulnerability in tumors that resistant to such therapy. Further validation in patient-derived models and clinical samples is required. In addition, the discontinuation of MRTX1133 development limits the direct clinical relevance of findings specific to this compound. Nevertheless, MRTX1133 served here as a pharmacological tool for investigating *KRAS*^{G12D} inhibitor resistance, and the relevance of the PYCR2-PP2Ac-eIF2α axis to other *KRAS*^{G12D}-targeted agents remains to be determined.

In conclusion, we identify PYCR2 as a novel regulator of sensitivity to *KRAS*^{G12D} -targeted therapy in CCA. Mechanistically, PYCR2 drives therapeutic resistance via PP2Ac-dependent eIF2α dephosphorylation and sustained protein translation. These findings deepen our understanding of adaptive resistance to *KRAS*-targeted therapies and indicate that disrupting the PYCR2-PP2Ac-eIF2α axis represents a promising strategy to improve the efficacy of *KRAS* inhibitor therapy in CCA.

Abbreviations

CCA: cholangiocarcinoma; co-IP: co-immuno precipitation; eIF2α: eukaryotic translation initiation factor 2α; GI_{50}: half-maximal growth inhibitory concentration; qPCR: quantitative PCR; P5C: pyrroline-5-carboxylate; PP2A: protein phosphatase; PP2Ac: Protein phosphatase 2A catalytic subunit; PYCR2: Pyrroline-5-carboxylate reductase 2.

Supplementary Material

Supplementary figures and tables 1, 3, 4.
https://www.ijbs.com/v23p0042s1.pdf
Supplementary table 2.
https://www.ijbs.com/v23p0042s2.xlsx

Acknowledgements

We thank all members of our research group for their valuable contributions.

Funding

This work was supported by the National Natural Science Foundation of China (82588201, 32270814, 82473208, 92359301, 81672371 and 82373223), Shanghai Science and Technology Industry High-Quality Development Plan-"Biomedical Innovation and Development" Project (25S11903600) and Shanghai Science and Technology Committee Rising-Star Program (24QA2711800).

Ethics approval and consent to participate

The animal study protocol was approved by the Experimental Animal Ethics Committee of the Naval Military Medical University.

Availability of data and material

All datasets associated with this study are available from the corresponding author upon reasonable request.

Author contributions

Liwei Dong, Tianyi Jiang and Hongyang Wang jointly supervised the research.

Huibo Feng and Mengmiao Pei conducted experiments and wrote original draft.

Huibo Feng, Mengyou Xu and Zhongning Yu analyzed the data.

Taiyu Shang, Lu Chen, Yuanyuan Zhang, Yunkai Lin and Yufei Pan provided expert consultation.

Xinhao Xing and Xinzhu Quan assisted with the experiments.

Competing Interests

The authors have declared that no competing interest exists.

References

1. Moris D, Palta M, Kim C, Allen PJ, Morse MA, Lidsky ME. Advances in the treatment of intrahepatic cholangiocarcinoma: An overview of the current and future therapeutic landscape for clinicians. CA Cancer J Clin. 2023; 73: 198-222.
2. Banales JM, Marin JJG, Lamarca A, Rodrigues PM, Khan SA, Roberts LR, et al. Cholangiocarcinoma 2020: the next horizon in mechanisms and management. Nat Rev Gastroenterol Hepatol. 2020; 17: 557-88.
3. Oh DY, Ruth He A, Qin S, Chen LT, Okusaka T, Vogel A, et al. Durvalumab plus Gemcitabine and Cisplatin in Advanced Biliary Tract Cancer. NEJM Evid. 2022; 1: EVIDoa2200015.
4. Woods E, Le D, Jakka BK, Manne A. Changing Landscape of Systemic Therapy in Biliary Tract Cancer. Cancers (Basel). 2022; 14.
5. Jusakul A, Cutcutache I, Yong CH, Lim JQ, Huang MN, Padmanabhan N, et al. Whole-Genome and Epigenomic Landscapes of Etiologically Distinct Subtypes of Cholangiocarcinoma. Cancer Discov. 2017; 7: 1116-35.
6. Hallin J, Bowcut V, Calinisan A, Briere DM, Hargis L, Engstrom LD, et al. Anti-tumor efficacy of a potent and selective non-covalent KRAS(G12D) inhibitor. Nat Med. 2022; 28: 2171-82.
7. Dilly J, Hoffman MT, Abbassi L, Li Z, Paradiso F, Parent BD, et al. Mechanisms of Resistance to Oncogenic KRAS Inhibition in Pancreatic Cancer. Cancer Discov. 2024; 14: 2135-61.
8. Shao DD, Xue W, Krall EB, Bhutkar A, Piccioni F, Wang X, et al. KRAS and YAP1 converge to regulate EMT and tumor survival. Cell. 2014; 158: 171-84.
9. Genovese G, Carugo A, Tepper J, Robinson FS, Li L, Svelto M, et al. Synthetic vulnerabilities of mesenchymal subpopulations in pancreatic cancer. Nature. 2017; 542: 362-6.
10. Wu G, Qin S, Gu K, Zhou Y. PYCR2, induced by c-Myc, promotes the invasiveness and metastasis of breast cancer by activating AKT signalling pathway. Int J Biochem Cell Biol. 2024; 166: 106506.
11. Luo MY, Zhou Y, Gu WM, Wang C, Shen NX, Dong JK, et al. Metabolic and Nonmetabolic Functions of PSAT1 Coordinate Signaling Cascades to Confer EGFR Inhibitor Resistance and Drive Progression in Lung Adenocarcinoma. Cancer Res. 2022; 82: 3516-31.
12. Alvarez ME, Savouré A, Szabados L. Proline metabolism as regulatory hub. Trends Plant Sci. 2022; 27: 39-55.
13. Fichman Y, Gerdes SY, Kovács H, Szabados L, Zilberstein A, Csonka LN. Evolution of proline biosynthesis: enzymology, bioinformatics, genetics, and transcriptional regulation. Biol Rev Camb Philos Soc. 2015; 90: 1065-99.
14. Shang T, Jiang T, Tan J, Jiang H, Xu M, Pan Y, et al. The noncanonical function of liver-type phosphofructokinase potentiates the efficacy of HDAC inhibitors in cancer. Signal Transduct Target Ther. 2025; 10: 341.
15. Dong L, Lu D, Chen R, Lin Y, Zhu H, Zhang Z, et al. Proteogenomic characterization identifies clinically relevant subgroups of intrahepatic cholangiocarcinoma. Cancer Cell. 2022; 40: 70-87.e15.
16. Sogabe S, Kamada Y, Miwa M, Niida A, Sameshima T, Kamaura M, et al. Crystal Structure of a Human K-Ras G12D Mutant in Complex with GDP and the Cyclic Inhibitory Peptide KRpep-2d. ACS Med Chem Lett. 2017; 8: 732-6.
17. Hu CA. Isozymes of P5C reductase (PYCR) in human diseases: focus on cancer. Amino Acids. 2021; 53: 1835-40.
18. Li Y, Bie J, Song C, Liu M, Luo J. PYCR, a key enzyme in proline metabolism, functions in tumorigenesis. Amino Acids. 2021; 53: 1841-50.
19. Raggi C, Taddei ML, Rae C, Braconi C, Marra F. Metabolic reprogramming in cholangiocarcinoma. J Hepatol. 2022; 77: 849-64.
20. Kuo ML, Lee MB, Tang M, den Besten W, Hu S, Sweredoski MJ, et al. PYCR1 and PYCR2 Interact and Collaborate with RRM2B to Protect Cells from Overt Oxidative Stress. Sci Rep. 2016; 6: 18846.
21. Lama Tamang R, Kumar B, Patel SM, Thapa I, Ahmad A, Kumar V, et al. Pyrroline-5-Carboxylate Reductase-2 Promotes Colorectal Carcinogenesis by Modulating Microtubule-Associated Serine/Threonine Kinase-like/Wnt/β-Catenin Signaling. Cells. 2023; 12.
22. Chen X, Shi C, He M, Xiong S, Xia X. Endoplasmic reticulum stress: molecular mechanism and therapeutic targets. Signal Transduct Target Ther. 2023; 8: 352.
23. Tian X, Zhang S, Zhou L, Seyhan AA, Hernandez Borrero L, Zhang Y, et al. Targeting the Integrated Stress Response in Cancer Therapy. Front Pharmacol. 2021; 12: 747837.
24. Chuang HY, Cheng CH, Guo F, Yadav VK, Fong IH, Lin JW, et al. Super-enhancer PPP1R15B/EIF2A axis characterizes aggressive drug-tolerant persister cells in Glioblastoma. Biomed Pharmacother. 2025; 189: 118309.
25. Lee S, Jee HY, Lee YG, Shin JI, Jeon YJ, Kim JB, et al. PKR-Mediated Phosphorylation of eIF2a and CHK1 Is Associated with Doxorubicin-Mediated Apoptosis in HCC1143 Triple-Negative Breast Cancer Cells. Int J Mol Sci. 2022; 23.
26. Ghaddar N, Wang S, Woodvine B, Krishnamoorthy J, van Hoef V, Darini C, et al. The integrated stress response is tumorigenic and constitutes a therapeutic liability in KRAS-driven lung cancer. Nat Commun. 2021; 12: 4651.
27. Palam LR, Gore J, Craven KE, Wilson JL, Korc M. Integrated stress response is critical for gemcitabine resistance in pancreatic ductal adenocarcinoma. Cell Death Dis. 2015; 6: e1913.
28. Haanen TJ, 3rd, O'Connor CM, Narla G. Biased holoenzyme assembly of protein phosphatase 2A (PP2A): From cancer to small molecules. J Biol Chem. 2022; 298: 102656.
29. Sarais F, Krempien F, Koehn C, Brewing L, Classen CF, Walter M, et al. Targeting PP2A in cancer: an underrated option. J Exp Clin Cancer Res. 2025; 44: 295.
30. Cyran AM, Kleinegger F, Nass N, Naumann M, Haybaeck J, Arens C. Inhibition of EIF2α Dephosphorylation Decreases Cell Viability and Synergizes with Standard-of-Care Chemotherapeutics in Head and Neck Squamous Cell Carcinoma. Cancers (Basel). 2023; 15.
31. Xue JY, Zhao Y, Aronowitz J, Mai TT, Vides A, Qeriqi B, et al. Rapid non-uniform adaptation to conformation-specific KRAS(G12C) inhibition. Nature. 2020; 577: 421-5.
32. Zhu C, Guan X, Zhang X, Luan X, Song Z, Cheng X, et al. Targeting KRAS mutant cancers: from druggable therapy to drug resistance. Mol Cancer. 2022; 21: 159.
33. Lines CL, McGrath MJ, Dorwart T, Conn CS. The integrated stress response in cancer progression: a force for plasticity and resistance. Front Oncol. 2023; 13: 1206561.